EES Catalysis

ROYAL SOCIETY
OF CHEMISTRY

PAPER
Alexandros Katsaounis *et al.*
Dynamic control of DRM and RWGS reactions over Ru/YSZ
catalysts by applied potential: insights into mechanisms and
selectivity

Check for updates

Dynamic control of DRM and RWGS reactions over Ru/YSZ catalysts by applied potential: insights into mechanisms and selectivity

Andriana Lymperi, [iD] Alexandros K. Bikogiannakis, Georgios Kyriakou [iD] and Alexandros Katsaounis [iD] *

This study explores the electrochemical promotion of dry reforming of methane (DRM) and reverse water−gas shift (RWGS) reactions over a ruthenium (Ru) catalyst supported on yttria-stabilized zirconia (YSZ). Physicochemical properties were examined using a range of surface and structural characterization techniques. Ru remained metallic after reaction, with minor oxidation under high CO_2 concentrations. While carbon was detected under all conditions, only oxidizing environments led to the accumulation of oxidized species, indicating surface-bound intermediates. Catalytic behavior was investigated under reducing (P_{CH_4} = 4 kPa, P_{CO_2} = 1 kPa) and stoichiometric (P_{CH_4} = 1 kPa, P_{CO_2} = 1 kPa) conditions. DRM dominated under reducing conditions, while stoichiometric feeds led to competition between DRM and RWGS, showing inverted volcano behavior. Positive polarization (+1 V) enhanced CO production by improving CH_4 adsorption, while negative polarization (−1 V) suppressed DRM and favored RWGS. Electrochemical promotion of catalysis (EPOC) was quantified by measuring the rate enhancement ratios (ρ). Under reducing conditions, positive polarization increased DRM rates tenfold at low temperatures, with reduced effect at higher temperatures. In contrast, negative polarization suppressed DRM and promoted RWGS. Under stoichiometric conditions, both reactions were enhanced, with selectivity determined by the polarity of the applied potential. Transient experiments at 380 °C confirmed reversibility of EPOC and its ability to dynamically steer selectivity. Reactive oxygen uptake provided insight into electrochemically active surface area and promotion mechanisms. These findings demonstrate the potential of EPOC to modulate the H_2/CO ratio and tailor selectivity in reforming processes, with relevance to renewable energy and biogas utilization.

Broader context

The growing demand for sustainable carbon management calls for technologies that can convert CO_2 and CH_4 – two major greenhouse gases – into valuable fuels and chemicals. Dry reforming of methane (DRM) and the reverse water gas shift (RWGS) are attractive routes, but their high energy requirements and limited selectivity hinder practical deployment. In this study, we show that applying a small potential to Ru/YSZ catalysts enables real-time switching between DRM- and RWGS-dominated pathways under isothermal conditions. We demonstrate that positive potentials promote DRM with high CO selectivity, while negative potentials favour RWGS *via* formate intermediates. This dynamic electrochemical modulation reveals distinct mechanistic regimes and provides external control over carbon conversion routes without structural catalyst changes. Our findings offer a new paradigm for electrified catalysis that couples renewable electricity with carbon valorisation, paving the way for efficient and flexible power-to-fuel systems. These insights are valuable for catalyst design, reactor engineering, and the broader decarbonization agenda.

1. Introduction

The escalating reliance on fossil fuels in industrial sectors over recent decades has precipitated a global economic and environmental crisis that requires urgent attention and mitigation.[1,2] Gaseous pollutants, specifically carbon dioxide (CO_2) and methane (CH_4), which are the primary anthropogenic greenhouse gases contributing to climate change,[3,4] have increased by over 150% and 260%, respectively, compared to pre-industrial levels. As of 2023, their concentrations have reached approximately 420 ppm for CO_2 and 1934 ppb for CH_4.[3] In recognition of the severity of the enhanced greenhouse

Department of Chemical Engineering, University of Patras, Caratheodory 1, University Campus, GR-26504, Patras, Greece.
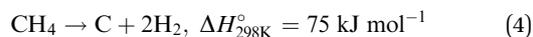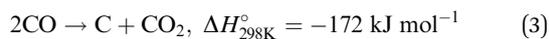*E-mail: alex.katsaounis@chemeng.upatras.gr*

effect and its role in driving climate change, both governmental bodies and the scientific community have initiated measures aimed at mitigating these impacts. The Paris Agreement,[5] endorsed by 195 nations, commits to limiting the average global temperature rise to well below 2 °C above pre-industrial levels. Additionally, the European Union has set a target to achieve net-zero emissions and carbon neutrality by 2050.[6]

The utilization of carbon-rich greenhouse gases as chemical feedstocks represents a highly promising and economically advantageous approach, as it simultaneously mitigates greenhouse gas emissions and enables the synthesis of valuable chemicals and fuels. Among the various reactions explored for this purpose, the dry reforming of methane (DRM) with carbon dioxide (eqn (1)) has garnered significant attention in recent years. This process exploits two of the most potent greenhouse gases –CO_2 and CH_4– to generate synthesis gas (syngas), a mixture of hydrogen (H_2) and carbon monoxide (CO) with a molar ratio of approximately 1:1. Syngas is an essential intermediate in chemical manufacturing, particularly as a precursor in the Fischer–Tropsch synthesis for the production of higher hydrocarbons and alcohols.[7] The H_2/CO ratio in syngas significantly influences product selectivity in downstream processes. A hydrogen-rich syngas composition tends to favor the formation of methane, light hydrocarbons, and lower alcohols, whereas a carbon monoxide-rich mixture promotes the synthesis of C_{5+} hydrocarbons and olefins.[8–11]

$$CH_4 + CO_2 \rightarrow 2CO + 2H_2, \quad \Delta H^{\circ}_{298K} = 248 \text{ kJ mol}^{-1} \quad (1)$$

$$CO_2 + H_2 \rightarrow CO + H_2O, \Delta H^{\circ}_{298K} = 41 \text{ kJ mol}^{-1} \quad (2)$$

Parallel to the DRM, carbon dioxide can also react with H_2 produced via the DRM process, yielding additional CO and water through the reverse water–gas shift (RWGS) reaction (eqn (2)). This reaction is mildly endothermic and is favored at lower temperatures, resulting in a decrease in the H_2/CO ratio to values below unity. In contrast, the DRM reaction is highly endothermic and requires elevated temperatures, typically above 700 °C, for optimal conversion.[12] Although these extreme conditions are advantageous for optimizing selectivity toward the DRM and achieving high reactant conversion, they also introduce significant economic and energy inefficiencies. Additionally, the elevated temperatures required for the DRM process can lead to catalyst deactivation, primarily through mechanisms such as sintering or carbon deposition, which substantially reduce the availability of active metal sites.[13–15] In this context, two primary reactions are responsible for carbon deposition: the Boudouard reaction (eqn (3)), which is thermodynamically favored at temperatures up to 700 °C, and the methane decomposition reaction (eqn (4)), which occurs at temperatures above 550 °C.[15–17]

$$2CO \rightarrow C + CO_2, \Delta H^{\circ}_{298K} = -172 \text{ kJ mol}^{-1} \quad (3)$$

$$CH_4 \rightarrow C + 2H_2, \Delta H^{\circ}_{298K} = 75 \text{ kJ mol}^{-1} \quad (4)$$

Nickel (Ni) catalysts are widely regarded as the benchmark for the DRM due to their high catalytic activity, excellent selectivity, low cost, and the metal's abundance.[16,18] Metal oxides, such as Al_2O_3, TiO_2, CeO_2, and SiO_2, are commonly employed as supports to enhance catalytic performance, improve dispersion, and mitigate agglomeration phenomena.[18–26] Other transition metals, including cobalt (Co) and copper (Cu), have also been utilized as DRM catalysts, yielding similarly favorable results, along with some bimetallic catalyst systems.[27–29] However, a significant drawback of these metals is their susceptibility to deactivation over time, primarily due to coke formation.[16,17] As a result, considerable research has been directed toward the use of noble metal catalysts.[13–15] Despite their higher cost, noble metals such as rhodium (Rh),[13,14,30–32] ruthenium (Ru),[13,14,30,33,34] and iridium (Ir)[13,35] have demonstrated superior reactivity, selectivity, and resilience to carbon deposition, making them highly reliable for the DRM process, even at lower reaction temperatures, and exhibiting remarkable stability in long-duration operation.

The majority of studies on the DRM are conducted in fixed-bed reactors, utilizing metal catalysts supported on metal oxide substrates in the form of powders. However, several investigations have explored the use of solid oxide fuel cell (SOFC) reactors for this purpose.[36–40] These reactors, operating at temperatures exceeding 700 °C, provide an ideal environment for the DRM reaction, and are primarily designed for energy production. In these systems, nickel (Ni) catalysts are commonly employed, deposited directly onto the solid electrolyte, typically Yttria-stabilized zirconia (YSZ)[41–52] or gadolinium-doped ceria (GDC).[41,49,51–54] These solid electrolytes function as oxygen ion (O^{2-}) conductors, and under closed-circuit conditions, the migration of oxygen ions to the catalyst surfaces can help mitigate carbon deposition. Additionally, the direct introduction of methane and carbon dioxide into the reactor obviates the need for an external reformer, enabling the simultaneous production of syngas and electricity.[51,52]

The proposed mechanisms for the DRM reaction vary depending on the catalyst, the metal oxide support, and the reaction conditions, with two primary reaction pathways commonly cited in the literature. For systems employing redox-active supports, the Langmuir–Hinshelwood–Hougen–Watson (LHHW) kinetic model is typically applied.[14,26,55–61] This bifunctional mechanism suggests that CO_2 is primarily adsorbed onto the support, while CH_4 adsorbs onto the active metal. The redox nature of the support facilitates the molecular adsorption of CO_2, leading to the formation of intermediate carbonate species and adsorbed oxygen. These carbonate species subsequently transform into adsorbed CO, while the adsorbed oxygen locally oxidizes the redox support. Methyl species, generated from the dissociative adsorption of methane on the catalyst surface, then react with the oxidized support to produce formate species, which eventually decompose into CO. The remaining hydrogen on the catalyst surface desorbs as molecular hydrogen. In this model, the rate-determining step is the activation of methane through hydrogen abstraction. Alternatively, the Langmuir–Hinshelwood model[14,55,56,62] suggests that both CO_2 and CH_4 are dissociatively adsorbed onto the catalyst surface. In this case, methane is fully dehydrogenated, and the adsorbed carbon reacts with oxygen derived from the decomposition of CO_2. However, catalytic systems following this pathway are prone to significant deactivation due to coke formation.

The majority of the experimental studies on the DRM reaction presented in the literature are conducted under high-temperature conditions, as these conditions are thermodynamically favorable. However, catalyst deactivation resulting from coke deposition, agglomeration, and the high operational costs associated with such systems hinder the industrial scalability of the DRM process. Consequently, the development of a catalytic system that can effectively operate at lower reaction temperatures, while achieving optimal H_2/CO ratios and efficient reactant conversion, is critical for advancing the DRM process.

A possible solution to the challenges associated with the DRM reaction is the application of the principles underlying the electrochemical promotion of catalysis (EPOC) phenomenon.[63,64] Also referred to as non-faradaic electrochemical modification of catalytic activity (NEMCA), EPOC offers an alternative to conventional chemical promotion and can be employed to enhance catalyst performance during polarization.[63–68] This technique involves the application of a constant electrical potential or current between a conductive catalyst film and a counter electrode, both deposited on a solid electrolyte. This setup induces the migration of ionic species to and from the catalyst surface. The electropositive or electronegative ions, derived from the solid electrolyte, act as promoting agents, which can be introduced to the catalyst surface in a controlled, predictable, and reversible manner at the three-phase boundary—where the catalyst, solid electrolyte, and reaction mixture interface. The migration of these ions leads to the formation of a neutral effective electrochemical double layer, which significantly modifies the catalyst's work function, Φ, by $\Delta\Phi = e \cdot \Delta U$.[63,69] This change in work function, in turn, alters the strength of the chemisorptive bonds between the reactant and intermediate species and the catalytic surface. Consequently, this alters the surface coverage of the catalyst, ultimately influencing catalytic activity and selectivity for various reactions.

The electrochemical promotion of catalysis (EPOC) phenomenon has been extensively studied for various catalytic reactions,[63,67] employing different solid electrolytes with varying ionic conductivities, such as O^{2-} ions for yttria-stabilized zirconia (YSZ),[70–73] titanium dioxide (TiO_2),[74] ceria (CeO_2),[75] H^+ ions for yttrium-doped barium zirconate (BZY),[76,77] and Na^+ and K^+ ions for β''-Al_2O_3.[78] Additionally, a wide range of catalysts have been investigated, including noble metals,[71,78–80] transition metals,[70,81] metal oxides,[82] bimetallic catalysts,[82,83] and nanoparticles.[76,80–82] In these studies, two primary parameters are typically used to quantify the EPOC effect,[63] as described by the following equations:

$$\rho = r/r_0 \tag{5}$$

$$\Lambda = \Delta r/I(n \cdot F) \tag{6}$$

Eqn (5) defines the rate enhancement ratio, ρ, which compares the electropromoted reaction rate, r, under polarization conditions to the catalytic rate, r_0, under open-circuit conditions. The apparent faradaic efficiency, Λ, given by eqn (6), quantifies the magnitude of the EPOC phenomenon by comparing the change in the catalytic rate during polarization, $\Delta r = r - r_0$, to the rate of ion migration to the catalytic surface, I/nF, where I is the applied current, n is the ion change, and F is the Faraday constant.

Based on the reaction rate behavior under negative and positive polarization conditions, four distinct types of behavior can be identified.[84] If the reaction rate increases with increasing applied potential, the reaction is classified as electrophobic. Conversely, if the reaction rate decreases with increasing applied potential, it is referred to as electrophilic. When the reaction rate reaches a maximum at a specific applied potential, the reaction is characterized as volcano-type. Finally, when the reaction rate increases for both negative and positive applied potentials, reaching a minimum, the reaction follows an inverted-volcano type behavior.

This study investigates the electrochemical promotion of the DRM reaction under low-temperature conditions. A ruthenium (Ru) catalyst is employed, as previous research has demonstrated its excellent stability and selectivity for the DRM reaction, while successfully suppressing the undesirable parallel RWGS reaction even under low temperature conditions with minimal catalyst deactivation.[14,30,55] Furthermore, previous EPOC studies have shown its stability under constant polarization conditions leading to limited electrochemical degradation and catalyst deactivation.[68,72,73] It is important to emphasize that Ni-based catalysts are widely acknowledged as the state-of-the-art materials for DRM, particularly under high-temperature conditions, due to their favorable activity and relatively low cost. However, one of the key challenges associated with Ni systems is their propensity toward carbon deposition and deactivation, especially at lower operating temperatures. In contrast, Ru-based catalysts, although more expensive, exhibit significantly higher resistance to coking and maintain high selectivity toward DRM over competing side reactions. In the present study, we emphasize these advantages by operating under comparatively mild conditions, where intrinsic kinetic effects can be directly probed.

The Ru catalytic film is deposited onto an yttria-stabilized zirconia (YSZ) solid electrolyte pellet, enabling the utilization of O^{2-} ions as promoters during polarization. These ions are introduced to the catalytic surface in a predictable and fully reversible way in order to alter the work function of the Ru catalyst resulting in activity and selectivity modifications, as well as protecting the catalyst from deactivation due to carbon deposition.[49,51] The primary objective of this study is twofold. First, the reaction is conducted under low-temperature conditions to reduce the high energy demands associated with temperatures above 700 °C. However, under these conditions, CH_4 and CO_2 conversion is significantly lower, DRM reaction is not thermodynamically favored, and selectivity is substantially shifted towards the RWGS reaction. To address this challenge, both positive and negative polarization potentials are applied to modulate selectivity towards the DRM reaction, suppress the RWGS pathway, and achieve a hydrogen-to-carbon monoxide (H_2/CO) ratio as close to unity as possible, while simultaneously increasing overall reactant conversion. A comprehensive kinetic investigation, complemented by both catalytic and electrocatalytic experiments, was conducted to achieve the aforementioned objectives. When benchmarked against reported low-temperature DRM systems, our Ru/YSZ catalyst demonstrates competitive or superior activity while

simultaneously suppressing the undesired RWGS pathway, particularly under electrochemical promotion. These findings underscore the potential of Ru/YSZ as a model system for exploring EPOC in DRM, while also providing insight into strategies that could enhance the performance of more economically viable catalysts, such as Ni. To the best of our knowledge, no similar study has been reported in the existing literature.

2. Results and discussion

2.1 Physicochemical characterization

The crystallinity, particle size distribution, and morphology of the Ru catalyst film were characterized by X-ray diffraction (XRD), scanning electron microscopy (SEM), and energy dispersive spectroscopy (EDS) analyses. As illustrated in Fig. 1, both fresh (post-reduction pre-treatment) and used (post-experimentation) Ru samples predominantly exist in their metallic state, as evidenced by well-defined reflections at 2θ angles of $38.8°$, $42.6°$, $44.5°$, $58.9°$, $70°$, and $79.2°$. A minor peak at $27.5°$ is also present in both samples, which can be attributed to trace amounts of RuO_2 remaining even after the reduction process or to minor oxidation of the Ru surface during sample transfer for XRD analysis. The diffraction peaks for the reduced Ru sample are sharper, indicating a smaller average crystallite size, which was estimated using Scherrer's equation to be 12.5 ± 1.2 nm. In contrast, the used sample exhibits a slightly larger average size of 14.3 ± 1.3 nm, indicative of mild sintering effects likely induced by prolonged operation at elevated temperatures and sustained electrochemical polarization. The remaining diffraction peaks are attributed to the YSZ solid electrolyte support.

SEM images of the fresh and used sample, shown in Fig. 2, reveal a highly porous microstructure consisting of Ru particle clusters. The fresh sample after the reduction pre-treatment step (Fig. 2(a) and (b)) appears to be quite uniform showing well-defined Ru particles creating a cohesive metallic film. The
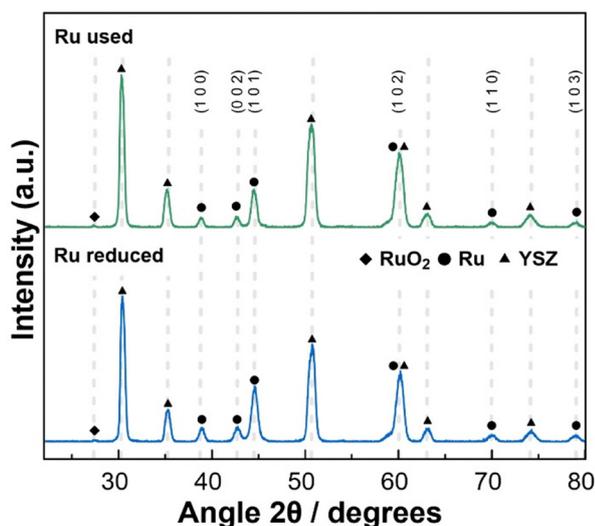

Fig. 1 XRD pattern of Ru film on YSZ after reduction pre-treatment (fresh sample) (bottom) and after all experiments (used sample) (top).

line scan analysis of the sample presented in Fig. S1 clearly demonstrates that the surface is composed of Zr and Y, that correspond to the YSZ pellet, and Ru which is the main domain. It is worth noting that even if the surface does not appear entirely uniform, the EDS analysis of the line scan clearly shows that the surface is predominantly covered by Ru particles, while the Zr and Y signals are very weak compared to the Ru one. The corresponding particle size distribution can be seen in Fig. 2(c). After measuring more than 500 particles form multiple SEM images, the mean particle size was 28.9 ± 9.3 nm, while the Ru nanoparticles appear to be mostly spherical.

Fig. S2(a) and (b) demonstrate a representative SEM image of the cross section of the catalytic sample paired with a line scan of the cross section, respectively. The SEM image shows a uniform thin Ru film with a thickness of around 500 nm. Ru nanoparticles seem to have infiltrated to the first few layers of the YSZ pellet, which have been corroborated by the line scan analysis of the cross section. Specifically, moving from right to left in Fig. S2(b), firstly, the Ru signal appears to be as high as 100% with weak signals of Y and Zr corresponding to the YSZ pellet. Moving further into the pellet, the Ru signal weakens and becomes almost comparable to that of Zr, indicating a limited region of metal diffusion into the solid electrolyte. After that, the Zr signal is dominant and there is almost no interaction between the solid electrolyte pellet and the Ru metallic film.

A very similar behavior to that of the fresh sample can be seen in Fig. 2(d) and (e). The used Ru sample maintained its porous nanostructure; however, some structural changes have been induced. The metallic film now consists of larger Ru clusters of small particles showing evidence of limited agglomeration phenomena after all experiments were conducted. Nevertheless, the spherical structure of the particles remains the same and the mean particle size increases only by little, 30.2 ± 11.4 nm (Fig. 2(f)). These observations are in great agreement with the XRD analysis of Fig. 1.

It should be noted here that these minimal structural changes, especially regarding the particle size distribution of Ru nanoparticles, are not consistent with existing literature on metal supported catalysts on redox supports.[85–88] Specifically, while in previous work Ru has been reported to undergo dynamic structural changes during the reaction, this was normally attributed to the redox nature of the support and not an inherent property of Ru. Since YSZ does not act as a redox support in the classical sense, only as a means for oxygen ion migration, profound structural changes are unlikely, as shown in the XRD and SEM images of the sample pre and post reaction.

Fig. S3 presents the EDS analysis of the Ru/YSZ sample, which confirms the presence of ruthenium, yttrium, zirconium, and oxygen in the used sample, with minimal carbon content, consistent with expectations after the completion of the experiments. Carbon presence in the sample was further validated through X-ray photoelectron spectroscopy (XPS) analysis.

Fig. 3 shows the XPS spectra of the Ru 3d region for the Ru catalyst sample after four different treatment conditions.
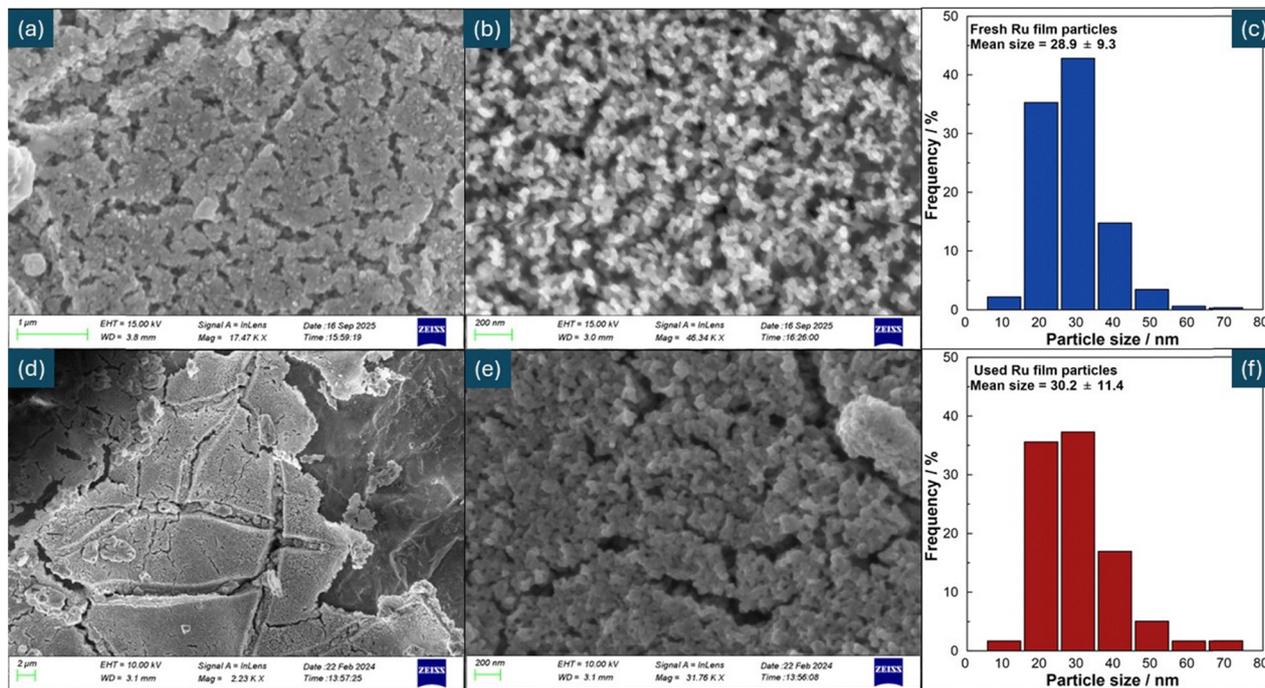
Fig. 2 SEM images of the Ru catalytic surface and the corresponding metal particle size distribution of the fresh-after reduction pre-treatment-sample (a), (b) and (c), and the used sample (d), (e) and (f).

Specifically, Ru/YSZ. 1 corresponds to the fresh after reduction sample, while Ru/YSZ. 2, 3 and 4 were obtained after 10 to 12 hours of experiment under reducing (P_{CO_2} = 1 kPa, P_{CH_4} = 4 kPa), stoichiometric (P_{CO_2} = 1 kPa, P_{CH_4} = 1 kPa) and oxidizing (P_{CO_2} = 2 kPa, P_{CH_4} = 1 kPa) conditions respectively. After the deconvolution of the obtained spectra, one can observe the asymmetric doublet Ru $3d_{5/2}$–Ru $3d_{3/2}$ at 280.0 and 284.1 eV respectively, confirming the Ru^0 metallic state of the catalytic film in all four samples. However, only when the sample is exposed to excess amounts of CO_2 (Ru/YSZ. 4), the oxidized state of Ru appears, with two additional peaks appearing at 280.7 and 284.8 eV. These peaks correspond to the RuO_2 structure resulting in the broadening of the Ru 3d doublet and its shift to slightly higher binding energies. The formation of these peaks provides evidence of the redox cycles that take place on the catalytic surface during the reaction. Specifically, the excess amount of CO_2 is capable of forming stable RuO_2 on the catalytic surface, whilst under all other conditions, while it is highly likely that under reaction conditions Ru undergoes redox cycles, these RuO_X species are unstable and dissolve under the reaction mixture. Moreover, in the same figure, one can observe the overlapping C 1s region. Comparing the reduced sample with those after reaction conditions, careful deconvolution reveals that the carbon content of the surface does not increase after reducing and stoichiometric conditions, as the intensity of the C 1s peak at 284.8 eV corresponding to C–C, C–H groups remains practically constant. However, after oxidizing conditions, the wider and stronger contribution for the apparent $3d_{3/2}$ peak, in combination with the evident tail formed at higher binding energies is evidence of carbon peaks that appear at 286.4 and 288.8 eV due to the formation of C=O and O–C=O groups, as well as the increased intensity of the

284.8 eV peak, confirming the acute carbon formation when excess amount of CO_2 is present in the reactant feed. The peaks arising from oxidized carbon species can be attributed to reactant intermediates which remain bonded to the catalytic surface. Finally,
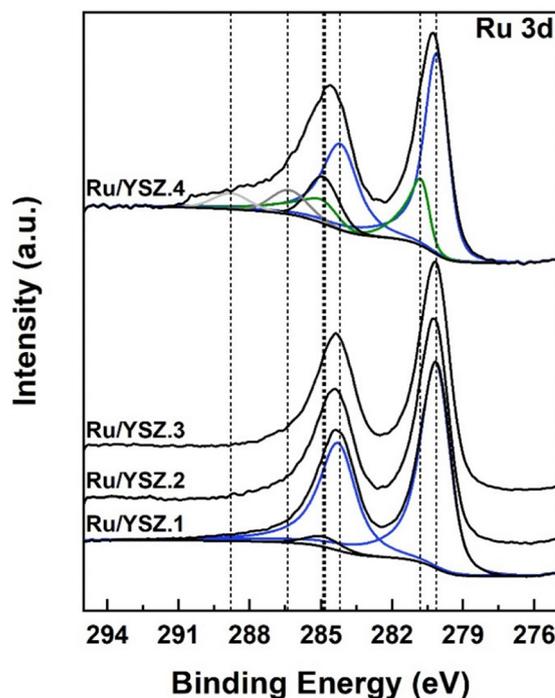

Fig. 3 XPS spectra of Ru 3d and C 1s region for the Ru film after being subjected to various treatments.

high resolution scans of the Cl 2p region (not shown here) revealed no presence of remnant chloride on the catalytic surface, following sample preparation. This extended XPS analysis confirms that Ru remains predominantly metallic under reducing and stoichiometric conditions, with stable RuO_2 features forming only under oxidizing conditions. These findings directly highlight the redox behavior of the Ru film during reaction and address the role of Ru oxidation states under different environments.

The combined SEM/EDS and XPS analyses confirm that the Ru layer remains structurally uniform and predominantly metallic under reaction conditions, with only limited oxidation observed in strongly oxidizing environments. This stability of Ru^0 is directly correlated with the observed high selectivity toward DRM over RWGS, underscoring the crucial role of the Ru/YSZ interface in maintaining catalytic performance during electrochemical promotion.

While the SEM results confirm that morphological restructuring of Ru is minimal under the investigated conditions, the XPS data suggest that dynamic changes in the oxidation state-particularly under electrochemical polarization-may play a more decisive role in governing the catalytic behavior, highlighting the central importance of redox-driven surface dynamics in the manifestation of the EPOC effect.

2.2 Catalytic results

Prior to conducting any electrocatalytic experiments, the catalytic activity of the Ru/YSZ pellet was evaluated. Initially, to identify the optimal volumetric flow rate that would maintain differential conditions without hindering catalyst conversion, the steady-state effect of the total gas mixture flow rate on the catalytic reaction rate was investigated. The experiment was performed under stoichiometric conditions (P_{CO_2} = 1 kPa, P_{CH_4} = 1 kPa) at a constant temperature of 400 °C. The methane and carbon dioxide consumption rates, as well as the production rates of carbon monoxide from DRM and the RWGS reactions, as a function of total gas flow rate, are presented in Fig. S4.

The data indicate that the reaction rates initially increase with increasing volumetric flow rate, reaching a plateau at a flow rate of 200 cm^3 min^{-1}. This plateau suggests that mass transfer effects become negligible beyond this flow rate, and therefore, a flow rate of 200 cm^3 min^{-1} was chosen for subsequent experiments.

Fig. 4(a) depicts the influence of CH_4 partial pressure on the rate of carbon monoxide (CO) production *via* the DRM and the RWGS reactions. In this analysis, the partial pressure of carbon dioxide and the reaction temperature were kept constant at 1 kPa and 400 °C, respectively. The data demonstrate a monotonic increase in CO production *via* the DRM pathway with increasing CH_4 concentration, indicating a positive reaction order with respect to CH_4 for the DRM reaction. Conversely, the CO production rate associated with the RWGS reaction initially increases, reaching a maximum at a CH_4 partial pressure of 2 kPa, beyond which a gradual decline is observed. This peak suggests that, under low CH_4 partial pressure conditions, competitive adsorption of CO_2 on the Ru catalyst surface facilitates its reaction with H_2 generated from DRM. However, as the CH_4 partial pressure continues to rise, the increased surface coverage of the catalyst by CH_4 likely inhibits CO_2 adsorption, in agreement with mechanistic studies indicating preferential adsorption of CH_4 over CO_2 on Ru-based active sites.[14,55,89] Consequently, the surface CO_2/H_2 ratio decreases, resulting in a diminished RWGS reaction rate despite the elevated H_2 production.

Fig. 4(b) illustrates the dependence of the reaction rates on CO_2 partial pressure, with the CH_4 partial pressure fixed at 1 kPa. Initially, both DRM and RWGS reaction rates increase
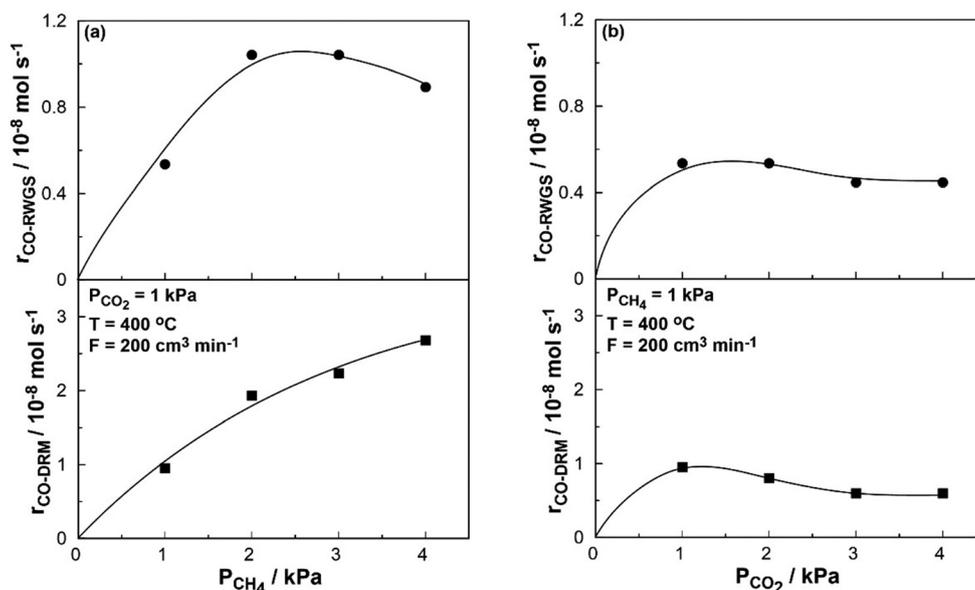

Fig. 4 Steady-state effect of the partial pressure of CH_4 (a) and CO_2 (b) on the catalytic rate of CO production during the DRM (bottom) and RWGS (top) reaction under open-circuit conditions (o.c.). T = 400 °C, F = 200 cm^3 min^{-1}.

with increasing CO_2 partial pressure. However, beyond a threshold of approximately 1 kPa, the reaction rates exhibit a negative dependence on CO_2 partial pressure, indicative of inhibitory effects at higher CO_2 concentrations.

According to the principles of electrochemical and chemical promotion,[84] the DRM reaction is predicted to be primarily electrophobic, as its rate is positively correlated with the electron-donor reactant (CH_4) and negatively correlated with the electron-acceptor reactant (CO_2). Conversely, at low CH_4 partial pressures and a stoichiometric reactant ratio, the RWGS reaction is expected to exhibit inverted volcano behavior, with its rate increasing with both electron-donor and electron-acceptor partial pressures. At higher partial pressures of both reactants, the reaction rate is anticipated to follow a volcano behavior, where the rate decreases with further increase in reactant concentrations.

2.3 Reaction conditions' selection

All catalytic and electropromoted experiments were conducted under reducing (P_{CO_2} = 1 kPa and P_{CH_4} = 4 kPa) and stoichiometric (P_{CO_2} = 1 kPa and P_{CH_4} = 1 kPa) conditions, which were chosen for several reasons. Firstly, kinetic experiments demonstrated that under reducing conditions, the system's selectivity shifts significantly towards the DRM reaction, which is beneficial as the primary objective of this study is to enhance the H_2/CO ratio. Furthermore, under stoichiometric conditions, both reactions are expected to exhibit inverted volcano behavior, as indicated by the kinetic study, leading to an overall improvement in reactant conversion during closed-circuit operation.

In prior catalytic studies on the dry reforming of methane over noble metal catalysts,[41,42,49] typically conducted at temperatures above 600 °C, a decrease in the CO_2/CH_4 ratio was shown to promote carbon deposition via methane decomposition. This led to the inevitable deactivation of the catalyst due to a significant reduction in the active sites on the catalyst surface. However, since the activation of the methane decomposition reaction occurs at temperatures higher than 550 °C,[15,16] the temperature range selected in this study eliminates this issue. The increased methane concentration in the feed mixture enhances the catalyst's surface coverage with methane, thus promoting a shift in selectivity towards the DRM reaction, as observed in the kinetic analysis.

Another important consideration is the availability of biogas, which can serve as the feed gas in similar studies. Biogas, a by-product of anaerobic biological waste treatment, typically contains 50–75% CH_4 and 25–50% CO_2, depending on the waste source.[90–92] Consequently, studying both stoichiometric and reducing conditions is particularly relevant, as biogas could be utilized as a raw material in dry reforming of methane processes, positioning it as a renewable energy source.[91]

Furthermore, using an inlet mixture with a high CO_2 concentration is less viable within the studied temperature range. Catalyst characterization by XPS (Fig. 3) revealed significant carbon deposition and gradual catalyst deactivation after extended experimental durations.

Finally, for the electrochemical promotion of the Ru catalyst, polarization at ±1 V was selected, as this potential was found to induce a pronounced promotional effect on both catalytic reactions, as discussed in the following section. Although the application of potentials significantly exceeding |1| V could, in principle, further enhance the rate of CO formation, such conditions introduce a considerable risk of structural degradation of the YSZ electrolyte, ultimately compromising both its mechanical integrity and its ionic/electronic conductivity.[93,94] Therefore, operating at 1 V constitutes an optimal compromise, as it ensures substantial electrochemical promotion of the Ru catalyst while simultaneously preserving the long-term structural and functional stability of the YSZ electrolyte.

2.4 Electrocatalytic results

Fig. S6(a) and Fig. 5(a) present the steady-state influence of temperature on the consumption rates and conversions of CH_4 and CO_2, as well as the CO production rate, via the DRM and the RWGS reactions under reducing conditions. These results are shown for open-circuit operation and under both anodic (U = +1 V) and cathodic (U = −1 V) polarization. Under open-circuit conditions, the reaction rates increase nearly monotonically with temperature, consistent with the endothermic nature of both DRM and RWGS reactions. Notably, the CO_2 consumption rate consistently exceeds that of CH_4, attributed to the concurrent RWGS reaction, in which CO_2 reacts with H_2 generated from DRM. Application of positive potential (+1 V) significantly enhances CO production via DRM. This enhancement is ascribed to the migration of O^{2-} ions from the solid electrolyte to the catalyst surface, which increases the Ru work function. Consequently, the adsorption strength of CH_4 (an electron donor) improves, leading to higher CH_4 surface coverage and promotion of the DRM reaction. Conversely, negative polarization (−1 V) depletes surface oxygen species and reduces the Ru work function, thereby strengthening the Ru–CO_2 interaction. This results in suppressed CO formation via DRM. For the RWGS reaction, only minor changes in reaction rates are observed under both polarization modes. While positive polarization increases H_2 production, the limited CO_2 surface coverage on Ru inhibits RWGS activity. In contrast, negative polarization enhances CO_2 adsorption but is accompanied by a marked reduction in H_2 availability, yielding a similar suppression of RWGS.

Fig. S6(b) and Fig. 5(b) illustrate the temperature dependence of reaction rates under stoichiometric feed conditions. Compared to reducing conditions, the overall conversions are substantially lower, primarily due to the excess methane in the feed, which results in nearly threefold greater conversion of the limiting reactant (CO_2). Under open-circuit and positive polarization (U = +1 V), the temperature-dependent trends in reaction rates are qualitatively similar to those observed under reducing conditions. However, under negative polarization (U = −1 V), a markedly different behavior emerges. At temperatures below 360 °C, all reaction rates approach zero, indicating a near-complete suppression of the DRM reaction. Above 360 °C, both CH_4 and CO_2 consumption rates increase, with CO_2 consumption exhibiting a steeper rise. This suggests that both DRM and RWGS reactions are promoted at elevated temperatures under
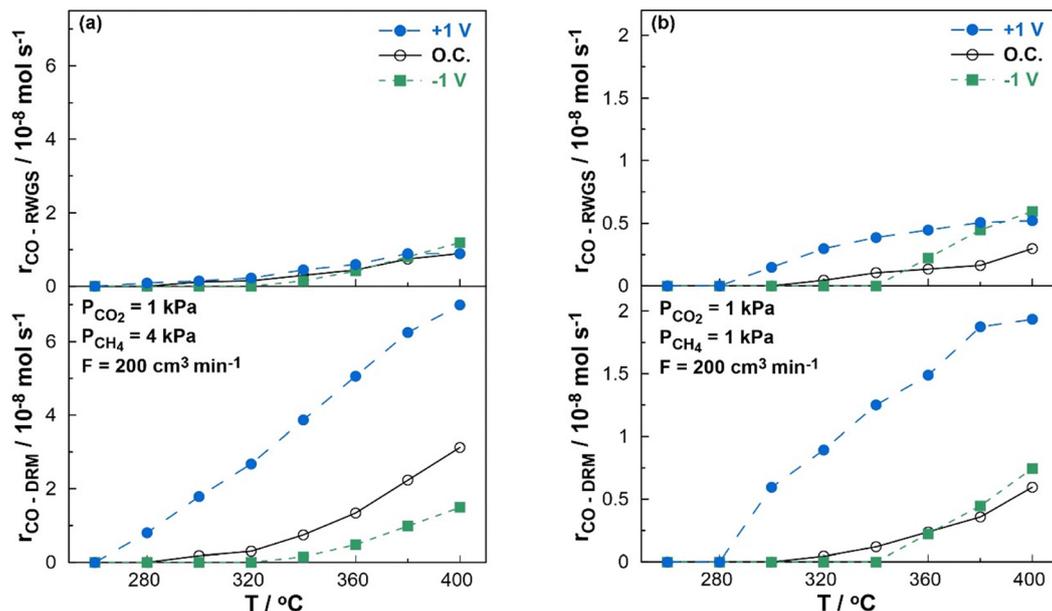
Fig. 5 Steady-state effect of temperature on the catalytic rate of CO production during the DRM reaction (bottom) and RWGS reaction (top) under open-circuit (o.c.), positive polarization (U_{WR} = +1 V) and negative polarization (U_{WR} = −1 V) conditions. (a) P_{CO_2} = 1 kPa, P_{CH_4} = 4 kPa (reducing conditions). (b) P_{CO_2} = 1 kPa, P_{CH_4} = 1 kPa (stoichiometric conditions). F = 200 cm^3 min^{-1}.

negative polarization, deviating significantly from the trends observed under reducing conditions. This shift indicates a complex interplay between temperature, feed composition, and polarization that modulates catalytic activity.

Fig. 6 presents the steady-state effect of temperature on the H_2/CO ratio. Under open-circuit conditions, the H_2/CO ratio increases with temperature, reaching values of 0.57 for reducing and 0.37 for stoichiometric conditions at 400 °C. When a positive potential is applied, the H_2/CO ratio experiences a substantial increase, achieving values as high as 0.8 and 0.6 for reducing and stoichiometric conditions, respectively, even at the lowest temperatures. Previous thermocatalytic studies[13–15,33] on DRM using

supported Ru catalysts suggest that such high selectivity toward DRM, reflected in elevated H_2/CO ratios, is typically only attainable at temperatures above 600 °C due to thermodynamic constraints. Even in studies[95–101] using the state-of-the-art catalyst for the DRM reaction, Ni, on different supports, the selectivity at such low temperatures shifts greatly towards the RWGS reaction resulting in low H_2/CO ratio. Similarly to the Ru supported catalysts, elevated temperatures, usually higher than 550 °C depending on the supported Ni catalyst, are suggested in order to achieve H_2/CO ratios as high as 0.6 under stoichiometric reaction conditions. However, the modification of the Ru catalyst work function by the migration of oxygen ions to the gas–catalyst–solid electrolyte
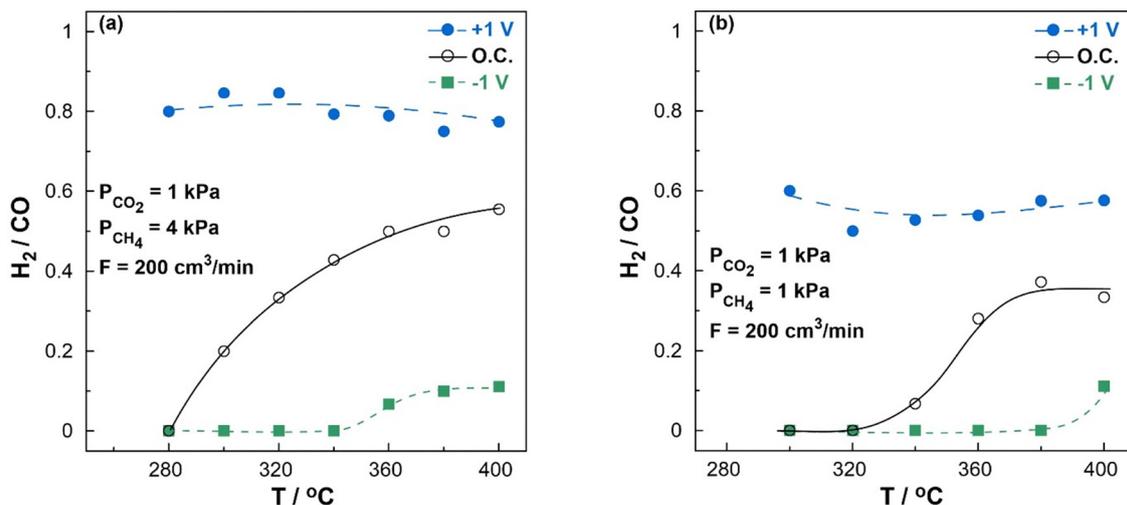

Fig. 6 Steady-state effect of temperature on the H_2/CO ratio under open-circuit (o.c.), positive polarization (U_{WR} = +1 V) and negative polarization (U_{WR} = −1 V) conditions. (a) P_{CO_2} = 1 kPa, P_{CH_4} = 4 kPa (reducing conditions). (b) P_{CO_2} = 1 kPa, P_{CH_4} = 1 kPa (stoichiometric conditions). F = 200 cm^3 min^{-1}.

interface leads to the formation of an adsorbed CH_4 "barrier." This barrier impedes further reaction of the limited CO_2 with the H_2 produced from the DRM reaction, significantly suppressing the RWGS pathway and thereby enhancing the H_2/CO ratio.

In contrast, negative polarization shifts the system's selectivity dramatically, such that the majority of the H_2 produced from the DRM reaction is consumed in the RWGS reaction for further CO production, resulting in a reduction in the H_2/CO ratio. Under certain conditions, particularly at lower temperatures, the DRM reaction can be nearly completely suppressed, leading to no H_2 production, and the RWGS reaction is unable to proceed due to the absence of its limiting reactant. This phenomenon is evident in Fig. 5, where, at temperatures as low as 320 °C for reducing and 340 °C for stoichiometric conditions, no CO is produced under negative polarization, despite lower light-off temperatures observed under open-circuit conditions.

To quantify the electrochemical enhancement of the reaction rates presented in Fig. 5 and Fig. S6, the rate enhancement ratio, ρ, is utilized. Fig. 7 displays the steady-state temperature dependence of the rate enhancement ratio for CO production *via* the DRM and RWGS reactions.

Under reducing conditions (Fig. 7(a)), the rate enhancement ratio for the DRM reaction reaches a maximum value of 10, indicating a tenfold increase in the reaction rate at the lowest temperature with the application of a positive potential (+1 V). As temperature increases, the rate enhancement gradually decreases, reaching a value of $\rho_{CO} = 2$ at 400 °C. However, as shown in Fig. 6(a), despite the reduced overall promotion of CO production at higher temperatures, the H_2/CO ratio remains exceptionally high across the studied temperature range. Application of a negative potential significantly suppresses the DRM reaction, with the rate enhancement ratio approaching zero. At

temperatures above 360 °C, the system's selectivity shifts entirely to the RWGS reaction, where the rate enhancement ratio for CO production *via* RWGS exceeds unity. Regarding the RWGS reaction, application of a positive potential consistently increases the reaction rate compared to open-circuit conditions, although the enhancement never exceeds 50% ($\rho_{RWGS} < 1.5$).

Under stoichiometric conditions (Fig. 7(b)), the rate enhancement of both DRM and RWGS reactions is notably higher, with ρ values of 30 and 10, respectively, at the lowest temperature. As with reducing conditions, the promotion of both reactions diminishes with increasing temperature, with $\rho_{DRM} = 3.25$ and $\rho_{RWGS} = 1.75$ at 400 °C. Interestingly, negative polarization also exerts a beneficial effect on both reactions. Below 360 °C, no CO is produced due to complete suppression of the DRM reaction; however, at higher temperatures, the rate enhancement ratio increases, with a 25% increase in the DRM rate ($\rho_{DRM} = 1.25$) and a 100% increase in the RWGS rate ($\rho_{RWGS} = 2$) at the highest temperature.

Fig. 8 illustrates the transient effect of the continuous application of both positive and negative potentials on the consumption rates and conversion of CH_4 and CO_2, as well as the total CO production rate, at a constant temperature of 380 °C. The corresponding current response is also shown in the figure.

Under open-circuit conditions (Fig. 8(a), excess CH_4), the total CO production rate initially stabilizes at approximately 3×10^{-8} mol s^{-1}, with a corresponding H_2/CO ratio of 0.5. At all times, the CO_2 consumption rate is higher than that of CH_4, as CO_2 is also consumed in the parallel RWGS reaction. Upon application of a positive potential (+1 V), which induces the migration of oxygen ions (O^{2-}) onto the Ru catalyst surface,
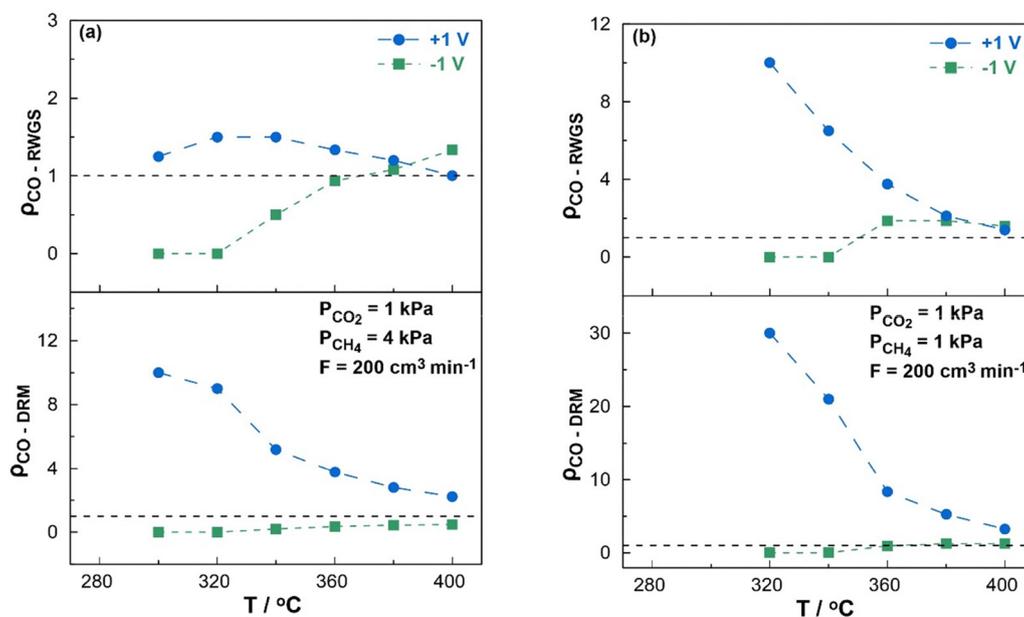

Fig. 7 Steady-state effect of temperature on the rate enhancement ratio, ρ, of the DRM (bottom) and RWGS (top) reaction under open-circuit (o.c.), positive polarization ($U_{WR} = +1$ V) and negative polarization ($U_{WR} = -1$ V) conditions. (a) $P_{CO_2} = 1$ kPa, $P_{CH_4} = 4$ kPa (reducing conditions). (b) $P_{CO_2} = 1$ kPa, $P_{CH_4} = 1$ kPa (stoichiometric conditions). $F = 200$ cm^3 min^{-1}.
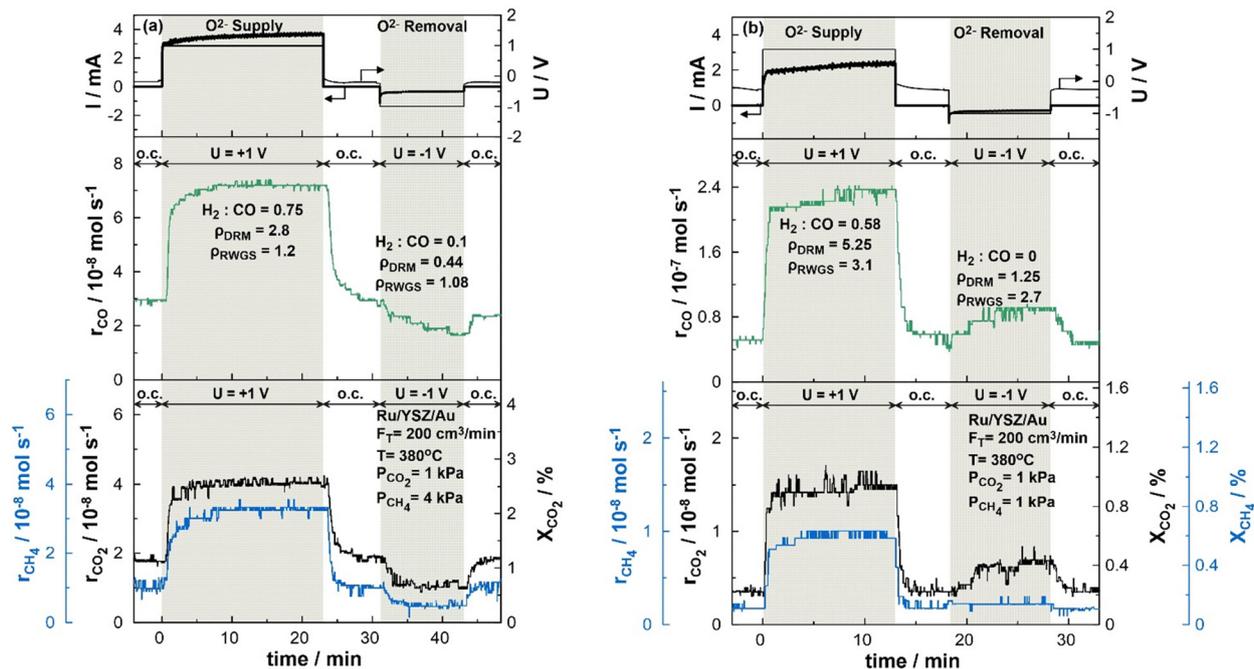
Fig. 8 Transient effect of constant applied positive (+1 V) and negative (−1 V) potential on the catalytic rate of CO_2 and CH_4 consumption (bottom left), conversion of limiting reactant (bottom right), total CO production (middle) and produced current (top left). (a) P_{CO_2} = 1 kPa, P_{CH_4} = 4 kPa (reducing conditions). (b) P_{CO_2} = 1 kPa, P_{CH_4} = 1 kPa (stoichiometric conditions). F = 200 cm³ min⁻¹, T = 380 °C.

there is a significant increase in CO production, accompanied by higher consumption rates of both CH_4 and CO_2. This migration of O^{2-} ions increases the catalyst work function (Φ), thereby strengthening the adsorption of CH_4 (electron donor) to the catalyst surface. Consequently, CO production increases rapidly, reaching a rate of 7.15×10^{-8} mol s⁻¹, and the reaction system's selectivity shifts toward the DRM reaction, resulting in a H_2/CO ratio of 0.75. The corresponding rate enhancement ratios for the DRM and RWGS reactions under these conditions are 2.8 and 1.2, respectively, indicating electrochemical promotion of both reactions.

In contrast, application of a negative potential leads to the migration of oxygen ions away from the catalyst surface, resulting in a decrease in the catalyst's work function. This enhances the Ru–CO_2 adsorption bond and shifts the system's selectivity toward the RWGS reaction, resulting in a decrease in the total CO production rate. Under these conditions, the H_2/CO ratio is reduced to 0.1, with rate enhancement ratios of 0.44 for the DRM reaction and 1.08 for the RWGS reaction. Upon interruption of the applied potential, all reaction rates return to their initial values, confirming the reversibility of the electrochemical promotion of catalysis (EPOC) phenomenon.

Under stoichiometric conditions (Fig. 8(b)), the application of a positive potential yields results comparable to those observed under reducing conditions. Specifically, the total CO production rate increases from 0.5×10^{-8} to 2.4×10^{-8} mol s⁻¹, with the H_2/CO ratio rising to 0.58, relative to the open-circuit value of 0.35. This enhancement reflects a more pronounced promotion of both reactions, with the DRM and RWGS reaction rates increasing by factors of 5.25 and 3.1, respectively.

In contrast, negative polarization induces a distinct behavior. Under these conditions, the equimolar CH_4/CO_2 feed appears to facilitate a more extensive promotion of CO production via both reaction pathways (ρ_{DRM} = 1.25 and ρ_{RWGS} = 2.7). Although the product distribution again shifts in favor of the RWGS pathway (as indicated by an H_2/CO ratio approaching zero), the increased availability of CO_2 allows for more effective adsorption on the Ru catalytic surface. This, in turn, promotes its subsequent reaction with the H_2 produced, resulting in an overall increase in CO production.

The potentiostatic transient profiles (Fig. 8) may also be employed to estimate the reactive oxygen uptake (N_G) of the Ru catalyst, which serves as a measure of the active catalytic surface area. This estimation is based on the determination of the relaxation time constant (τ), defined as the time required for the rate enhancement (Δr) to reach 63% of its final steady-state value. Assuming a 1:1 stoichiometry between surface metal active sites and adsorbed oxygen atoms, the following equation can be applied to calculate the magnitude of τ:

$$\tau = 2FN_G/I. \qquad (7)$$

Here, I denotes the steady-state current observed following the application of potential, and F is the Faraday constant. Using eqn (7) and the transient response under positive polarization at 380 °C (as shown in Fig. 8), the relaxation time constant (τ) was estimated to be approximately 33 s under reducing conditions and 17 s under stoichiometric conditions. These values correspond to a reactive oxygen uptake (N_G) on the order of $\sim 10^{-7}$ mol O, which is consistent with previously reported values in the literature.[63,72,73,77]

The steady-state effect of the applied potential on CO production *via* the DRM and RWGS reactions, along with the corresponding H_2/CO product ratio at a constant temperature of 380 °C, is presented in Fig. 9. The associated CH_4 and CO_2 consumption rates, conversions, and product selectivities as a function of applied potential are shown in Fig. S8. The open-circuit potential (OCP) was measured to be approximately −0.2 V. Prior to the onset of CO production in all experiments, the OCP exhibited positive values around +0.1 V. However, as the temperature increased and approached the light-off point, the potential dropped rapidly to a minimum negative value, coinciding with the initiation of CO formation. Ultimately, the potential stabilized at values between −0.4 V and −0.1 V, depending on the reaction temperature-with lower temperatures corresponding to more negative open-circuit potentials.

As shown in Fig. 9(a), the CO production rate *via* the DRM pathway increases significantly with increasing applied potential under reducing conditions, accompanied by a parallel rise in the H_2/CO ratio. In contrast, the RWGS reaction rate displays only minor changes as a function of applied potential, exhibiting a slight decline under both anodic and cathodic polarization. These results suggest that DRM exhibits electrophobic behavior, whereas RWGS follows a volcano-type trend with respect to applied potential. This interpretation is further supported by Fig. 10(a), which illustrates the rate enhancement ratios of the two reactions as functions of the applied potential. Notably, the RWGS reaction shows a peak near the open-circuit potential, with the rate enhancement ratio diminishing as the potential deviates in either direction, thereby reinforcing the characterization of RWGS as displaying volcano-type electrochemical behavior.

Under stoichiometric conditions (Fig. 9(b)), the potential-dependent behavior of the DRM and RWGS reactions exhibits a distinct deviation from that observed under reducing conditions. Although the H_2/CO ratio continues to increase with more positive applied potentials, similar to the trend under reducing conditions, the reaction rates of both DRM and RWGS follow a different pattern. Specifically, CO production *via* the DRM reaction increases under both anodic and cathodic polarization, with a more pronounced enhancement at positive potentials. A comparable trend is observed for the RWGS reaction, where the CO production rate also rises on either side of the potential axis. These findings are further corroborated by the data presented in Fig. 10(b), which illustrates the rate enhancement ratios under stoichiometric conditions. The symmetric increase in reaction rates at both positive and negative potentials indicates an inverted volcano-type behavior for both the DRM and RWGS pathways, suggesting that moderate deviations from the open-circuit potential, regardless of direction, promote surface reactivity under stoichiometric feeds.

3. Experimental

3.1 Catalyst preparation

A pellet-shaped solid electrolyte consisting of 8% Y_2O_3-stabilized ZrO_2, supplied by Ceraflex, was used, with a diameter of 18 mm and a thickness of 2 mm. The counter and reference electrodes were deposited on one side of the pellet using an organometallic gold paste (Metalor Au201 Gold Resinate 24%), followed by calcination at 450 °C for 30 min and 700 °C for 60 min. On the opposite side, a ruthenium (Ru) catalytic film,
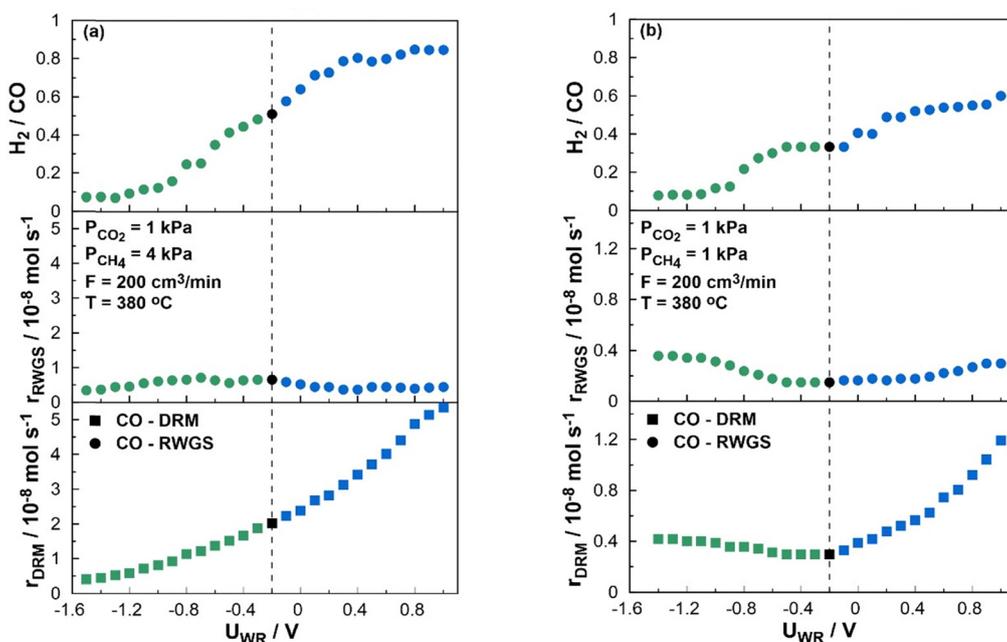

Fig. 9 Steady-state effect of applied potential on the catalytic rate of CO production during the DRM (bottom) and RWGS (middle) reaction and the H_2/CO ratio (top). (a) P_{CO_2} = 1 kPa, P_{CH_4} = 4 kPa (reducing conditions). (b) P_{CO_2} = 1 kPa, P_{CH_4} = 1 kPa (stoichiometric conditions). F = 200 cm^3 min^{-1}, T = 380 °C.
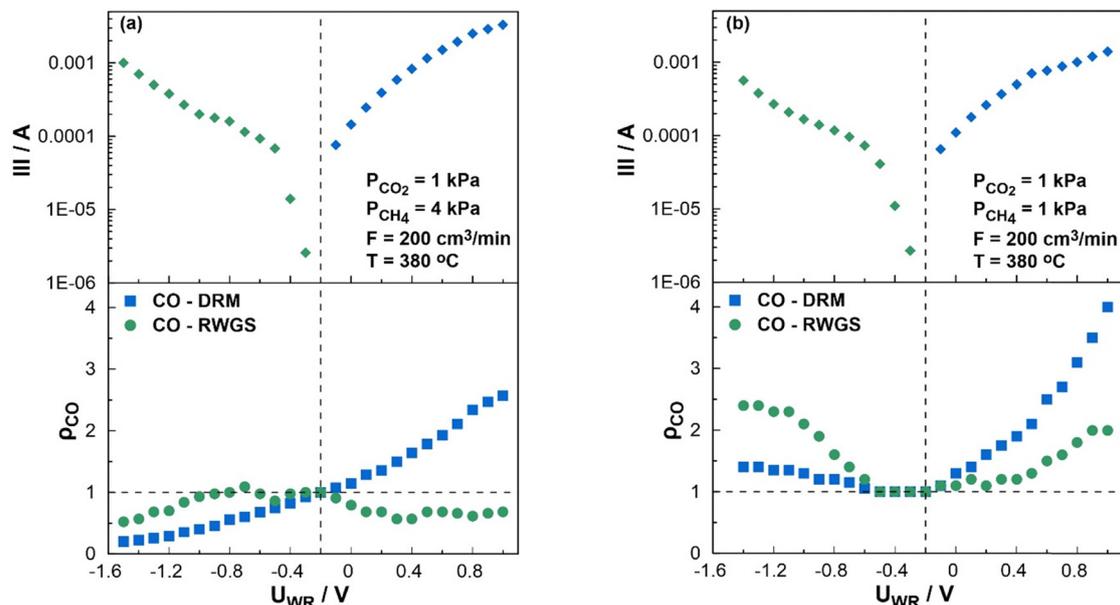
Fig. 10 Steady-state effect of applied potential on the rate enhancement ratio of CO, ρ (bottom) and the produced current (Tafel plot, top). (a) P_{CO_2} = 1 kPa, P_{CH_4} = 4 kPa (reducing conditions). (b) P_{CO_2} = 1 kPa, P_{CH_4} = 1 kPa (stoichiometric conditions). F = 200 cm³ min⁻¹, T = 380 °C.

which also served as the working electrode, was deposited through a two-step process. First, a 100 mM $RuCl_3$ isopropanol solution was applied dropwise at room temperature, followed by calcination at 500 °C for 60 min. Then, a reduction pretreatment was performed using a 15% H_2 in He mixture at 400 °C for 3 h. The final catalyst mass was 1.3 mg.

3.2 Reactor configuration and operation

All catalytic and electrocatalytic experiments were conducted in a continuous-flow, single-chamber reactor, as depicted in Fig. 11. The reactor consists of a quartz tube with a volume of 70 cm³, which is secured to a stainless-steel head using a Viton O-ring to ensure a tight seal. A stainless-steel water-cooling coil is attached to the metallic head to prevent overheating of the O-ring. The head also incorporates built-in ports for the inlet

and outlet gas streams, as well as a glass socket for a K-type thermocouple. The reactor inlet is positioned in close proximity to the solid electrolyte pellet and, particularly to the working electrode/catalyst, to ensure a highly turbulent flow around this region. As a result, the reactor can resemble a well-mixed CSTR type reactor close to the pellet. For the connection of the solid electrolyte to an external power source, three or more gold wires are routed through separate pockets in a ceramic tube positioned centrally within the metallic head. These gold wires are then wrapped around two ceramic rods that form the holder for the solid electrolyte pellet, thereby securing the pellet in a fixed position at the center of the reactor. Each gold wire is in contact with the corresponding electrode deposited on the solid electrolyte pellet. The reactor is placed within a quartz furnace to achieve the desired reaction temperature, which is monitored
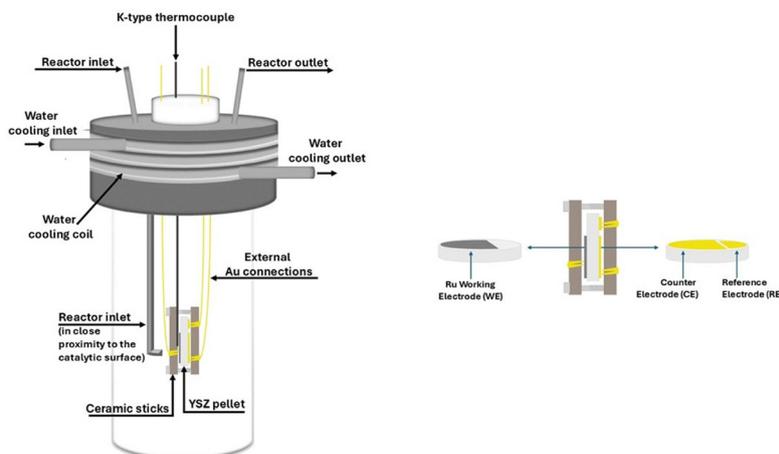

Fig. 11 Schematic representation of the single chamber reactor and solid electrolyte component.

using the K-type thermocouple positioned near the pellet for accurate temperature readings.

Electronic flowmeters from Brooks Instruments were used to regulate the total flow rate and gas feed composition. Certified gas mixtures, including 5% CH_4/He (Sol Group), 5% CO_2/He (Linde Hellas), and 99.999% He (Linde Hellas), were combined to achieve the desired reactant ratios. All experiments were conducted under reducing ($P_{CO_2}:P_{CH_4} = 1:4$) and stoichiometric ($P_{CO_2}:P_{CH_4} = 1:1$) conditions, with a total flow rate of 200 cm^3 min^{-1}, at atmospheric pressure and temperatures ranging from 260 to 400 °C. The outlet gas mixture was analyzed using an infrared gas analyzer from Fuji Electric in conjunction with a Shimadzu GC-2010 Plus gas chromatograph, equipped with a ValcoPlot Molesieve column. Constant potentials and currents were applied using an Amel 7050 potentiostat–galvanostat.

3.3 Catalyst characterization

The characterization of the structure and morphology of the Ru catalytic film deposited on the YSZ solid electrolyte was carried out using X-ray diffraction (XRD) and scanning electron microscopy (SEM) techniques. Specifically, an X-ray diffractometer Siemens D500 equipped with Cu Ka radiation was used operated at 40 kV and 30 mA achieving wavelength of the incident radiation equal to $\lambda_{Cu\ Ka}$= 1.542 Å. The scanning angle ranged between $2\theta = 20–80°$ and the major peaks were identified in comparison with library values (JPCDS). A Zeiss Supra 35 field emission, variable pressure scanning electron microscope was used to obtain SEM images. The microscope was equipped with a Bruker AXS energy dispersive spectrometer (EDS).

The reduced and after reaction treatment samples were swiftly transported from the single pellet reactor to an Ultra high vacuum (UHV) system, in order to minimize exposure to atmospheric conditions. Following incorporation into the main UHV chamber, X-ray photoelectron spectroscopy (XPS) measurements took place, utilizing an AlKα anode (1486.6 eV) at settings of 12 kV potential and 20 mA emission current. Analysis of ejected photoelectrons took place with a Leybold LH EA11 electron energy analyzer, which was operated at 100 eV pass energy. Spectral analysis took place using the XPS PEAK 4.1 software. The Ru 3d peak deconvolution was performed as reported in,[102] following the subtraction of a Shirley background.

4. Conclusions

This study highlights the significant role of electrochemical promotion in enhancing the dry reforming of methane (DRM) and reverse water-gas shift (RWGS) reactions over a Ru/YSZ catalyst. By modulating the applied potential, significant shifts in both reaction selectivity and overall catalytic efficiency were observed. Under anodic polarization, CO production *via* the DRM pathway increased substantially, primarily due to enhanced CH_4 adsorption, thereby shifting the reaction selectivity toward DRM and resulting in a higher H_2/CO ratio. In contrast, cathodic polarization promoted CO_2 adsorption, favoring the RWGS pathway while concurrently suppressing DRM activity. The observed electrocatalytic effects were fully reversible, confirming the dynamic and non-permanent nature of electrochemical promotion. Kinetic and transient analyses revealed that, under reducing conditions, DRM activity was strongly enhanced, whereas RWGS exhibited only marginal improvement. Under stoichiometric feed conditions, both DRM and RWGS reactions were promoted electrochemically, with positive potentials favoring DRM and negative potentials enhancing RWGS performance.

In contrast to conventional catalytic systems with fixed activity and selectivity, the electrochemically promoted Ru/YSZ catalyst enables dynamic, reversible tuning between DRM and RWGS pathways, offering precise control over product distribution, H_2/CO ratio and enhanced performance at lower temperatures. The utilization of a scaled-up monolithic electrochemically promoted type reactor (MEPR)[103] can eliminate the low reactants' conversion problem that was present in this study, leading to a more industrially applicable solution. Moreover, the results highlight the potential of biogas, a renewable and sustainable methane source, as a viable feedstock for low-temperature reforming processes. In contrast to previous EPOC studies, this work leads a pathway to the practical use of a renewable fuel for the on-site production of syngas and its direct integration into industrial processes. The application of electrochemical promotion thus presents a promising avenue for advancing methane reforming technologies toward more energy-efficient and environmentally sustainable solutions.

Conflicts of interest

The authors declare no conflicts of interest.

Data availability

All the data supporting this article are included in the main manuscript and the supplementary information (SI). Supplementary information is available. See DOI: https://doi.org/10.1039/d5ey00242g.

Acknowledgements

References

1 A. C. Ranveer, P. Pawar and P. T. Latake, *Int. J. Innovative Res. Creative Technol.*, 2016, **1**, 333–337.
2 Intergovernmental Panel on Climate Change (IPCC), Climate Change 2021 – The Physical Science Basis, 2023.
3 World Meteorological Organization, WMO Greenhouse Gas Bulletin (GHG Bulletin) – No. 17, 2021, vol. 17.

4 Intergovernmental Panel on Climate Change (IPCC), Climate Change 2022 – Impacts, Adaptation and Vulnerability, 2023.

5 United Nations, Paris Agreement - UNFCCC, 2015.

6 European Parliament, Official Journal of the European Union.

7 P. Zhai, Y. Li, M. Wang, J. Liu, Z. Cao, J. Zhang, Y. Xu, X. Liu, Y. W. Li, Q. Zhu, D. Xiao, X. D. Wen and D. Ma, *Chem*, 2021, **7**, 3027–3051.

8 M. Ding, Y. Yang, Y. Li, T. Wang, L. Ma and C. Wu, *Appl. Energy*, 2013, **122**, 1241–1246.

9 M. Lualdi, S. Lögdberg, M. Boutonnet and S. Järås, *Catal. Today*, 2013, **214**, 25–29.

10 N. Amirov and A. R. Vakhshouri, *Int. J. Hydrogen Energy*, 2020, **45**, 31913–31925.

11 A. Lillebø, E. Rytter, E. A. Blekkan and A. Holmen, *Ind. Eng. Chem. Res.*, 2017, **56**, 13281–13286.

12 F. Schrenk, L. Lindenthal, H. Drexler, G. Urban, R. Rameshan, H. Summerer, T. Berger, T. Ruh, A. K. Opitz and C. Rameshan, *Appl. Catal., B*, 2022, **318**, 121886.

13 M. Rezaei, S. M. Alavi, S. Sahebdelfar and Z.-F. Yan, *J. Nat. Gas Chem.*, 2006, **15**, 327–334.

14 A. Androulakis, I. V. Yentekakis and P. Panagiotopoulou, *Int. J. Hydrogen Energy*, 2023, **48**, 33886–33902.

15 D. Pakhare and J. Spivey, *Chem. Soc. Rev.*, 2014, **43**, 7813–7837.

16 F. Sharifianjazi, A. Esmaeilkhanian, L. Bazli, S. Eskandarinezhad, S. Khaksar, P. Shafiee, M. Yusuf, B. Abdullah, P. Salahshour and F. Sadeghi, *Int. J. Hydrogen Energy*, 2022, **47**, 42213–42233.

17 L. Baharudin, N. Rahmat, N. H. Othman, N. Shah and S. S. A. Syed-Hassan, *J. CO2 Util.*, 2022, **61**, 102050.

18 Z. Qin, J. Chen, X. Xie, X. Luo, T. Su and H. Ji, *Environ. Chem. Lett.*, 2020, **18**, 997–1017.

19 P. K. Chaudhary, N. Koshta and G. Deo, *Int. J. Hydrogen Energy*, 2020, **45**, 4490–4500.

20 M. Shah, M. K. Al Mesfer and M. Danish, *Int. J. Hydrogen Energy*, 2022, **47**, 8867–8874.

21 Z. He, K. Gong, Y. Dai, Q. Niu, T. Lin and L. Zhong, *J. Fuel Chem. Technol.*, 2024, **52**, 1203–1213.

22 Z. Qin, L. Chen, J. Chen, T. Su and H. Ji, *Greenhouse Gases: Sci. Technol.*, 2021, **11**, 1245–1264.

23 M. A. Vasiliades, C. M. Damaskinos, M. Lykaki, S. Stefa, V. D. Binas, T. Kentri, S. Boghosian, M. Konsolakis and A. M. Efstathiou, *Appl. Catal., B*, 2024, **350**, 123906.

24 Z. Ou, J. Ran, H. Qiu, X. Huang and C. Qin, *Fuel*, 2023, **335**, 126994.

25 Y. Zhang, G. Zhang, J. Liu, T. Li, Y. Wang, Y. Zhao, G. Li and Y. Zhang, *Fuel*, 2023, **340**, 127490.

26 A. M. Becerra, M. E. Iriarte and A. E. Castro-Luna, *React. Kinet. Catal. Lett.*, 2003, **79**, 119–125.

27 A. R. O. Sousa, A. J. M. Araujo, G. S. Souza, J. P. F. Grilo, F. J. A. Loureiro, D. P. Fagg and D. A. Macedo, *Mater. Lett.*, 2017, **191**, 141–144.

28 I. V. Yentekakis, P. Panagiotopoulou and G. Artemakis, *Appl. Catal., B*, 2021, **296**, 120210.

29 S. Chen, J. Zaffran and B. Yang, *Appl. Catal., B*, 2020, **270**, 118859.

30 V. A. Kondratenko, U. Karimova, A. A. Kasimov and E. V. Kondratenko, *Appl. Catal., A*, 2021, **619**, 118143.

31 Y. Beltrán, C. Fernández, G. Pecchi and R. Jiménez, *React. Kinet., Mech. Catal.*, 2016, **120**, 459–475.

32 I. V. Yentekakis, G. Goula, M. Hatzisymeon, I. Betsi-Argyropoulou, G. Botzolaki, K. Kousi, D. I. Kondarides, M. J. Taylor, C. M. A. Parlett, A. Osatiashtiani, G. Kyriakou, J. P. Holgado and R. M. Lambert, *Appl. Catal., B*, 2019, **243**, 490–501.

33 C. Egawa, *J. Catal.*, 2018, **358**, 35–42.

34 A. K. Bikogiannakis, A. Lymperi, P. Dimitropoulos, K. Bourikas and G. Kyriakou, *Molecules*, 2025, **30**, 2135.

35 E. Nikolaraki, G. Goula, P. Panagiotopoulou, M. J. Taylor, K. Kousi, G. Kyriakou, D. I. Kondarides, R. M. Lambert and I. V. Yentekakis, *Nanomaterials*, 2021, **11**, 2880.

36 L. Yan, L. Jiang, C. Qian and S. Zhou, *Energy Res.*, 2024, **3**, 100065.

37 S. A. Saadabadi, A. Thallam Thattai, L. Fan, R. E. F. Lindeboom, H. Spanjers and P. V. Aravind, *Renewable Energy*, 2019, **134**, 194–214.

38 S. Sengodan, R. Lan, J. Humphreys, D. Du, W. Xu, H. Wang and S. Tao, *Renewable and Sustainable Energy*, 2018, **82**, 761–780.

39 P. Qiu, S. Sun, X. Yang, F. Chen, C. Xiong, L. Jia and J. Li, *Int. J. Hydrogen Energy*, 2021, **46**, 25208–25224.

40 M. A. Abdelkareem, W. H. Tanveer, E. T. Sayed, M. E. H. Assad, A. Allagui and S. W. Cha, *Renewable Sustainable Energy Rev.*, 2019, **101**, 361–375.

41 A. Lanzini and P. Leone, *Int. J. Hydrogen Energy*, 2010, **35**, 2463–2476.

42 S. A. Saadabadi, B. Illathukandy and P. V. Aravind, *Energy Sci. Eng.*, 2021, **9**, 1232–1248.

43 G. Goula, V. Kiousis, L. Nalbandian and I. V. Yentekakis, *Solid State Ionics*, 2006, **177**, 2119–2123.

44 M. Pillai, Y. Lin, H. Zhu, R. J. Kee and S. A. Barnett, *J. Power Sources*, 2010, **195**, 271–279.

45 J. Staniforth and R. M. Ormerod, Implications for using biogas as a fuel source for solid oxide fuel cells: internal dry reforming in a small tubular solid oxide fuel cell, *Catal. Lett.*, 2002, **81**, 19–23.

46 M. Santarelli, F. Quesito, V. Novaresio, C. Guerra, A. Lanzini and D. Beretta, *J. Power Sources*, 2013, **242**, 405–414.

47 M. Chlipała, P. Błaszczak, S. F. Wang, P. Jasiński and B. Bochentyn, *Int. J. Hydrogen Energy*, 2019, **44**, 13864–13874.

48 H. Zhang, W. Liu, J. Wang, J. Yang, Y. Chen, W. Guan and S. C. Singhal, *J. Power Sources*, 2021, **516**, 230662.

49 T. Papadam, G. Goula and I. V. Yentekakis, *Int. J. Hydrogen Energy*, 2012, **37**, 16680–16685.

50 D. J. Moon and J. W. Ryu, *Catal. Today*, 2003, **87**, 255–264.

51 I. V. Yentekakis, G. Goula and T. Papadam, *Recent Progress in Computational Sciences and Engineering*, 2019.

52 I. V. Yentekakis, T. Papadam and G. Goula, *Solid State Ionics*, 2008, **179**, 1521–1525.

53 I. V. Yentekakis, *J. Power Sources*, 2006, **160**, 422–425.

54 F. J. A. Loureiro, G. S. Souza, V. C. D. Graça, A. J. M. Araújo, J. P. F. Grilo, D. A. Macedo and D. P. Fagg, *J. Power Sources*, 2019, **438**, 227041.

55 P. Ferreira-Aparicio, I. Rodríguez-Ramos, J. A. Anderson and A. Guerrero-Ruiz, *Appl. Catal., A*, 2000, **202**, 183–196.

56 K. Wittich, M. Krämer, N. Bottke and S. A. Schunk, *ChemCatChem*, 2020, **12**, 2130–2147.

57 J. Xu and G. F. Froment, *AIChE J.*, 1989, **35**, 88–96.

58 Z. L. Zhang and X. E. Verykios, *Catal. Today*, 1994, **21**, 589–595.

59 Y. A. Zhu, D. Chen, X. G. Zhou and W. K. Yuan, *Catal. Today*, 2009, **148**, 260–267.

60 J. Wei and E. Iglesia, *J. Phys. Chem. B*, 2004, **108**, 4094–4103.

61 C. Papadopoulou, H. Matralis and X. Verykios, *Catalysis for Alternative Energy Generation*, Springer, New York, 2012, vol. 9781461403449, pp. 57–127.

62 E. Akpan, Y. Sun, P. Kumar, H. Ibrahim, A. Aboudheir and R. Idem, *Chem. Eng. Sci.*, 2007, **62**, 4012–4024.

63 C. G. Vayenas, S. Bebelis, C. Pliangos, S. Brosda and D. Tsiplakides, *Electrochemical Activation of Catalysis. Promotion, Electrochemical Promotion and Metal-Support Interactions*, Kluwer Academic/Plenum Publishers, New York, 2001.

64 P. Vernoux, L. Lizarraga, M. N. Tsampas, F. M. Sapountzi, A. De Lucas-Consuegra, J. L. Valverde, S. Souentie, C. G. Vayenas, D. Tsiplakides, S. Balomenou and E. A. Baranova, *Chem. Rev.*, 2013, **113**, 8192–8260.

65 S. G. Neophytides, D. Tsiplakides, P. Stonehart, M. M. Jaksic and C. G. Vayenas, *Nature*, 1994, **370**, 45–47.

66 D. Tsiplakides and S. Balomenou, *Catal. Today*, 2009, **146**, 312–318.

67 A. Katsaounis, *J. Appl. Electrochem.*, 2010, **40**, 885–902.

68 C. G. Vayenas and C. G. Koutsodontis, *J. Chem. Phys.*, 2008, **128**, 182506.

69 C. G. Vayenas, S. Bebelis and S. Ladas, *Nature*, 1990, **343**, 625–627.

70 D. Zagoraios, N. Kokkinou, G. Kyriakou and A. Katsaounis, *Catal. Sci. Technol.*, 2022, **12**, 1869–1879.

71 A. Lymperi, C. Chatzilias, F. Xydas, E. Martino, G. Kyriakou and A. Katsaounis, *Nanomaterials*, 2023, **13**, 1930.

72 C. Chatzilias, E. Martino, C. G. Vayenas, G. Kyriakou and A. Katsaounis, *Appl. Catal., B*, 2022, **317**, 121778.

73 D. Theleritis, S. Souentie, A. Siokou, A. Katsaounis and C. G. Vayenas, *ACS Catal.*, 2012, **2**, 770–780.

74 C. Pliangos, I. V. Yentekakis, S. Ladas and C. G. Vayenas, *J. Catal.*, 1996, **159**, 189–203.

75 P. D. Petrolekas, S. Balomenou and C. G. Vayenas, *J. Electrochem. Soc.*, 1998, **145**, 1202.

76 D. Zagoraios, C. Panaritis, A. Krassakopoulou, E. A. Baranova, A. Katsaounis and C. G. Vayenas, *Appl. Catal., B*, 2020, **276**, 119148.

77 I. Kalaitzidou, A. Katsaounis, T. Norby and C. G. Vayenas, *J. Catal.*, 2015, **331**, 98–109.

78 M. Makri, A. Katsaounis and C. G. Vayenas, *Electrochim. Acta*, 2015, **179**, 556–564.

79 N. Kokkinou, F. Xydas, S. Brosda, G. Kyriakou and A. Katsaounis, *Catalysts*, 2023, **13**, 1014.

80 I. Kalaitzidou, D. Zagoraios, S. Brosda, A. Katsaounis, P. Vernoux and C. G. Vayenas, *Mater. Today: Proc.*, 2018, **5**, 27345–27352.

81 D. Zagoraios, S. Tsatsos, S. Kennou, C. G. Vayenas, G. Kyriakou and A. Katsaounis, *ACS Catal.*, 2020, **10**, 14916–14927.

82 D. Zagoraios, A. Athanasiadi, I. Kalaitzidou, S. Ntais, A. Katsaounis, A. Caravaca, P. Vernoux and C. G. Vayenas, *Catal. Today*, 2020, **355**, 910–920.

83 N. Ahledel, K. K. Saini, M. Couillard and E. A. Baranova, *ChemCatChem*, 2024, **16**, e202301363.

84 C. G. Vayenas, S. Brosda and C. Pliangos, *J. Catal.*, 2001, **203**, 329–350.

85 Z. Liu, F. Zhang, N. Rui, X. Li, L. Lin, L. E. Betancourt, D. Su, W. Xu, J. Cen, K. Attenkofer, H. Idriss, J. A. Rodriguez and S. D. Senanayake, *ACS Catal.*, 2019, **9**, 3349–3359.

86 Y. Li, T. Qin, J. Wei, J. Xiong, P. Zhang, K. Lai, H. Chi, X. Liu, L. Chen, X. Yu, Z. Zhao, L. Li and J. Liu, *Nat. Commun.*, 2023, **14**, 7149.

87 A. Aitbekova, L. Wu, C. J. Wrasman, A. Boubnov, A. S. Hoffman, E. D. Goodman, S. R. Bare and M. Cargnello, *J. Am. Chem. Soc.*, 2018, **140**, 13736–13745.

88 Z. Y. Zhang, J. L. Yao, Y. Q. Pan, D. M. Su, M. J. Cao, X. J. Gong, T. Li, L. Chen and T. Xie, *Nano Energy*, 2025, **133**, 110474.

89 N. Li, X. Li, R. Pan, M. Cheng, J. Guan, J. Zhou, M. Liu, J. Tang and D. Jing, *ChemPhotoChem*, 2021, **5**, 748–757.

90 P. G. Kougias and I. Angelidaki, *Front. Environ. Sci. Eng.*, 2018, 12.

91 L. Xie, J. Xu, Y. Zhang and Y. He, *Adv. Bioenergy*, 2020, **5**, 309–344.

92 S. Jung, J. Lee, D. H. Moon, K. H. Kim and E. E. Kwon, *Renewable Sustainable Energy Rev.*, 2021, **143**, 110949.

93 R. E. W. Casselton, *J. Appl. Electrochem.*, 1974, **4**, 25–28.

94 M. Jovaní, H. Beltrán-Mir, E. Cordoncillo and A. R. West, *Sci. Rep.*, 2019, **9**, 18538.

95 B. Abdullah, N. A. Abd Ghani and D. V. N. Vo, *J. Cleaner Prod.*, 2017, **162**, 170–185.

96 M. Yusuf, A. S. Farooqi, L. K. Keong, K. Hellgardt and B. Abdullah, *Chem. Eng. Sci.*, 2021, **229**, 116072.

97 Y. Wang, L. Yao, S. Wang, D. Mao and C. Hu, *Fuel Process. Technol.*, 2018, **169**, 199–206.

98 R. Patel, A. H. Fakeeha, S. O. Kasim, M. L. Sofiu, A. A. Ibrahim, A. E. Abasaeed, R. Kumar and A. S. Al-Fatesh, *Mol. Catal.*, 2021, **510**, 111676.

99 S. Andraos, R. Abbas-Ghaleb, D. Chlala, A. Vita, C. Italiano, M. Laganà, L. Pino, M. Nakhl and S. Specchia, *Int. J. Hydrogen Energy*, 2019, **44**, 25706–25716.

100 Y. Wang, L. Yao, Y. Wang, S. Wang, Q. Zhao, D. Mao and C. Hu, *ACS Catal.*, 2018, **8**, 6495–6506.

101 V. La Parola, L. F. Liotta, G. Pantaleo, M. L. Testa and A. M. Venezia, *Appl. Catal., A*, 2022, **642**, 118704.

102 D. J. Morgan, *Surf. Interface Anal.*, 2015, **47**, 1072–1079.

103 C. Chatzilias, E. Martino, A. Katsaounis and C. G. Vayenas, *Appl. Catal., B*, 2021, **284**, 119695.